Optical and Near-infrared Observations of the Distant but Bright 'New Year's Burst' GRB 220101A

Zi-Pei Zhu, Wei-Hua Lei, Daniele B Malesani, Shao-Yu Fu, Dong-Jie Liu, Dong Xu, Paolo d'Avanzo, José Feliciano Agüí Fernández, Johan P.U Fynbo, Xing Gao, et al.

The Astrophysical Journal, 959:118 (12pp), 2023 December 20 https://doi.org/10.3847/1538-4357/ad05c8

Optical and Near-infrared Observations of the Distant but Bright "New Year's Burst" GRB 220101A

Zi-Pei Zhu[1,2], Wei-Hua Lei[2], Daniele B. Malesani[3,4], Shao-Yu Fu[1,5], Dong-Jie Liu[2], Dong Xu[1], Paolo D'Avanzo[6], José Feliciano Agüí Fernández[7], Johan P. U. Fynbo[3,8], Xing Gao[9], Ana Nicuesa Guelbenzu[10], Shuai-Qing Jiang[1,5], David Alexander Kann[7,11], Sylvio Klose[10], Jin-Zhong Liu[1,9], Xing Liu[1,12], Massimiliano De Pasquale[13], Antonio de Ugarte Postigo[14], Bringfried Stecklum[10], Christina Thöne[15], Joonas Kari Markku Viuho[3,8], Yi-Nan Zhu[16], Jin-Da Li[17], He Gao[17], Tian-Hua Lu[1,5], Shuo Xiao[18], Yuan-Chuan Zou[2], Li-Ping Xin[1], and Jian-Yan Wei[1,5]

[1] Key Laboratory of Space Astronomy and Technology, National Astronomical Observatories, Chinese Academy of Sciences, Beijing, 100101, People's Republic of China; dxu@nao.cas.cn
[2] Department of Astronomy, School of Physics, Huazhong University of Science and Technology, Wuhan, 430074, People's Republic of China; leiwh@hust.edu.cn
[3] Niels Bohr Institute, University of Copenhagen, Jagtvej 155, DK-2200, Copenhagen N, Denmark
[4] Department of Astrophysics/IMAPP, Radboud University, P.O. Box 9010, 6500 GL, The Netherlands
[5] School of Astronomy and Space Science, University of Chinese Academy of Sciences, Chinese Academy of Sciences, Beijing 100049, People's Republic of China
[6] Brera Astronomical Observatory, via Bianchi 46, I-23807, Merate (LC), Italy
[7] Instituto de Astrofísica de Andalucía, Glorieta de la Astronomía s/n, E-18008 Granada, Spain
[8] The Cosmic Dawn Centre (DAWN), Denmark
[9] Xinjiang Astronomical Observatory, Chinese Academy of Sciences, Urumqi, Xinjiang 830011, People's Republic of China
[10] Thüringer Landessternwarte Tautenburg, D-07778 Tautenburg, Germany
[11] Hessian Research Cluster ELEMENTS, Giersch Science Center, Max-von-Laue-Strasse 12, Goethe University Frankfurt, Campus Riedberg, D-60438 Frankfurt am Main, Germany
[12] Key Laboratory of Cosmic Rays, Ministry of Education, Tibet University, Lhasa, Tibet 850000, People's Republic of China
[13] University of Messina, Mathematics, Informatics, Physics and Earth Science Department, via F.D. D'Alcontres 31, Polo Papardo, I-98166, Messina, Italy
[14] Université Côte d'Azur, Observatoire de la Côte d'Azur, Artemis, CNRS, F-06304 Nice, France
[15] Astronomical Institute of the Czech Academy of Sciences (ASU-CAS), Fričova 298, 251 65 Ondřejov, Czech Republic
[16] CAS Key Laboratory of Optical Astronomy, National Astronomical Observatories, Chinese Academy of Sciences, Beijing 100101, People's Republic of China
[17] Department of Astronomy, Beijing Normal University, Beijing 100875, People's Republic of China
[18] Key Laboratory of Particle Astrophysics, Institute of High Energy Physics, Chinese Academy of Sciences, 19B Yuquan Road, Beijing 100049, People's Republic of China

Received 2023 March 14; revised 2023 October 13; accepted 2023 October 16; published 2023 December 13

Abstract

High-redshift gamma-ray bursts (GRBs) are useful to probe the early Universe, but only a few candidates have been detected so far. Here, we report the optical and near-infrared observations of the afterglow of a relatively high-redshift event GRB 220101A, which was triggered on New Year's Day of 2022, and therefore referred to as the "New Year's burst." With the optical spectra obtained by XL2.16/BFOSC and NOT/ALFOSC, we determine the redshift of the burst to be $z = 4.615$. We find that the optical afterglow of GRB 220101A is one of the most luminous ever detected. Based on our optical and near-infrared data, and combined with the X-ray observations, we perform a multiband fit with the Python package *afterglowpy*. The jet opening angle is constrained to $\sim 3\overset{\circ}{.}4$, which is consistent with the jet-break time at ~ 0.7 day. We also determine the circumburst density of $n_0 = 0.15\ \mathrm{cm}^{-3}$ and kinetic energy $E_{\mathrm{K,iso}} = 3.5 \times 10^{54}$ erg. In the prompt phase of the burst, we find a "mirror" feature in the lightcurve from 80 s to 120 s. The physical origin of such a mirror feature is unclear.

Unified Astronomy Thesaurus concepts: Gamma-ray bursts (629)

1. Introduction

Gamma-ray bursts (GRBs) are the most energetic and luminous transient events in the Universe. The typical isotropic equivalent energy of GRBs is between 10^{50} and 10^{54} ergs, and the duration typically ranges from subseconds to several hundred seconds (Atteia et al. 2017). Based on the statistic of prompt emission T_{90} duration timescale and the spectral hardness of the bursts, GRBs are generally divided into two categories, i.e., short-hard bursts with $T_{90} < 2$ s, and long-soft bursts with $T_{90} < 2$ s. The short GRBs originate from neutron star–neutron star/black hole mergers and are associated with kilonovae (Kouveliotou et al. 1993; Zhang et al. 2009; Abbott et al. 2017). Long bursts come from the collapse of massive stars and are associated with broad-line Type Ic supernovae (Galama et al. 1999; Woosley & Bloom 2006). Meanwhile, there are also some confusing exceptions, i.e., GRB 060505 (Fynbo et al. 2006), GRB 060614 (Della Valle et al. 2006; Fynbo et al. 2006; Gehrels et al. 2006), GRB 200826A(Ahumada et al. 2021; Zhang et al. 2021), and GRB 211211A(Rastinejad et al. 2022).

After the first afterglow counterpart was discovered by BeppoSAX in the 1990s, the corresponding redshift was measured for the first time and the cosmological origin of GRBs was determined (see Zhang 2018, for a review). With the launch of the Neil Gehrels Swift Observatory (Swift hereafter) in 2004, more and more bursts have been detected with accurate positions (Gehrels et al. 2004). Nearly 600 bursts with redshifts (up to ~ 9.4) have been measured so far (Cucchiara et al. 2011).[19] The majority of bursts have a redshift of less than 3, with only a

[19] http://www.mpe.mpg.de/~jcg/grbgen.html

handful exceeding 4 (Gupta et al. 2022). High-redshift GRBs are an essential complementary probe of the early Universe, and they may lead us to the elusive Population III stars (Lamb & Reichart 2000; Salvaterra 2015; Sobral et al. 2015; Fryer et al. 2022). Over the past 20 years, only one high-redshift (i.e., $z \gtrsim 4$) burst has been detected annually, on average. Therefore, the detection of high-redshift GRBs remains of significant interest. For a single event, multiband observations are important to investigate the intrinsic properties of these high-redshift bursts. This is also a great help in studying whether such a burst is significantly different from other GRBs at lower redshifts.

Recently, a high-redshift, long duration, and energetic burst, GRB 220101A, was detected by Swift (Tohuvavohu et al. 2022). A rough estimation of the redshift was first made by using data from the Xinglong 2.16 m Telescope (Fu et al. 2022), and then from the Nordic Optical Telescope (NOT; Fynbo et al. 2022) and the Copernico Telescope (Tomasella et al. 2022). Ursi et al. (2022b) analyzed the high-energy observations obtained by AGILE in detail. Meanwhile, Mei et al. (2022) provided a joint multiband analysis of the burst from soft X-rays to high energies (up to ∼1 GeV). Jin et al. (2023) carried out a time-resolved analysis of the Swift/UVOT 150 s exposure of the burst and found a rapidly evolving optical/ultraviolet flare with an unprecedentedly high absolute AB magnitude of roughly −39.4.

Here, we report our optical and near-infrared observations of GRB 220101A. For our modeling, we use the open-source Python package *afterglowpy*, which adopts the numerical computation of structured jet afterglows (Ryan et al. 2020). This paper is organized as follows: we first describe our multiband observations and redshift measurements in Section 2, and then present the combined analysis of multiband data with the X-ray lightcurve in Section 3. Finally, we briefly discuss our results and summarize the conclusions in Sections 4 and 5, respectively. A standard cosmology model is adopted with $H_0 = 67.3\,\mathrm{km\,s^{-1}Mpc^{-1}}$, $\Omega_M = 0.315$, and $\Omega_\Lambda = 0.685$ (Planck Collaboration et al. 2014).

2. Observations and Data Reduction

Observations of GRB 220101A were first triggered by the Burst Alert Telescope (BAT; Barthelmy et al. 2005) on board Swift at 05:09:55 UT on 2022 January 1 (Tohuvavohu et al. 2022) with a T_{90} (15−350 keV) of 173.36 ± 12.76 s (Markwardt et al. 2022). Observations were also triggered by other high-energy satellites such as Fermi/GBM (Lesage et al. 2022), Fermi/LAT (Arimoto et al. 2022), AGILE (Ursi et al. 2022a), and Konus-Wind (Tsvetkova et al. 2022). The X-ray Telescope (XRT; Barthelmy et al. 2005) started observations 80.8 s after the BAT trigger and found a bright, uncataloged X-ray source within the BAT error circle (Osborne et al. 2022). At about 9 s, the Ultra-Violet/Optical Telescope (UVOT; Roming et al. 2005) found a source with a white-band brightness of 14.7 at R.A., decl. (J2000) = $00^h05^m24\overset{s}{.}80$, $+31°46'08\overset{''}{.}4$, which is consistent with the XRT position (Kuin et al. 2022). Jin et al. 2023 analyzed the UVOT data in detail and found that the early lightcurve shows a rapidly evolving flare, which is interpreted as a reverse shock. In order to show the full lightcurve of the burst, we collected the white-band data from the work mentioned above. Meanwhile, we adopted the analysis results that the XRT repository produces (Evans et al. 2007, 2009) and downloaded the 0.3–10 keV unabsorbed lightcurve from the UK Swift Science Data Centre.[20] The early afterglow of the burst has been analyzed in detail by Jin et al. (2023); here, we focus on the analysis of the XRT data after 10 ks. We also noticed a mirror feature during the prompt emission and downloaded the time-tagged event (TTE) data from the Fermi Science Support Center's FTP site.[21] We selected the data from GBM NaI detectors n6 and n7 as they had the highest signal-to-noise ratios, extracted the 64 ms resolution counts data of both detectors, and merged them to form the lightcurve. The processing was done with the GBM Data Tools.[22] As we only need the photon counts of the lightcurve in Section 3.1, there was no further processing to convert the photon counts to flux density.

2.1. Hubble Space Telescope Observations

The Hubble Space Telescope (HST) observed the source on 2022 February 7 with the F125W and F775W filters on Wide-Field Camera 3 (Proposal ID: 16838; PI: Andrew S. Fruchter). We obtained the publicly available data from the Mikulski Archive for Space Telescopes (MAST) and measured the photometry using *photutils* (Bradley et al. 2021) with the point-spread function model constructed by *PSFEx* (Bertin 2011). Our photometric results are presented in Table 1. The F775W and F125W filters are treated as *i* and *J* filters, respectively, in the following analysis.

2.2. Ground-based Optical and Near-infrared Observations

We performed our multiband photometric follow-up with the following observatories: the Beijing Faint Object Spectrograph and Camera (BFOSC) on the Xinglong 2.16 m Telescope (Fan et al. 2016), the Ningbo Bureau Of Education And Xinjiang Observatory Telescope (NEXT; 0.6 m located at Xingming Observatory, China), the Alhambra Faint Object Spectrograph and Camera (ALFOSC) on the Nordic Optical Telescope (NOT; 2.56 m at the Roque de los Muchachos Observatory, La Palma, Spain), the Calar Alto Faint Object Spectrograph (CAFOS) on the Centro Astronómico Hispano en Andalucía (CAHA; 2.2 m telescope located at Calar Alto, Spain), the Near Infrared Camera Spectrometer (NICS) on the Telescopio Nazionale Galileo (TNG; 3.58 m telescope located on the Island of San Miguel del La Palma in the Canary Islands), the TAUtenburg KAMera (TAUKAM) 6×6 k CCD on the Tautenburg 1.34 m Schmidt Telescope (Stecklum et al. 2016), and the Espectrógrafo Multiobjeto Infra-Rojo (EMIR; on the Gran Telescopio CANARIAS (GTC) 10.4 m telescope). The celestial location of the burst is shown in Figure 1.

After standard data reduction with IRAF (Tody 1986) and astrometric calibration by *Astrometry.net* (Lang et al. 2010), the apparent photometric data were calibrated with the Sloan Digital Sky Survey (SDSS) 14th data release (Abolfathi et al. 2018), while the near-infrared data were calibrated with the 2MASS catalog (Skrutskie et al. 2006).[23] The Johnson–Cousin filters were calibrated with the converted magnitude from the Sloan system.[24] The details of the filters observed by these observatories and the photometric results are presented in Table 1 and shown in Figure 2.

[20] https://www.swift.ac.uk/xrt_curves/
[21] https://heasarc.gsfc.nasa.gov/FTP/fermi/data/gbm/bursts/
[22] https://fermi.gsfc.nasa.gov/ssc/data/analysis/gbm/
[23] https://irsa.ipac.caltech.edu/Missions/2mass.html
[24] https://www.sdss.org/dr12/algorithms/sdssUBVRITransform/#Lupton

Table 1
The Photometric Results of Our Observations Combined with Collected GCN Results

ΔT(day)	Telescope/Instrument	Filter	Mag (AB)	Ref.
0.219	Xinglong 2.16 m/BFOSC	*I*	17.76 ± 0.01	(1)
0.223	Xinglong 2.16 m/BFOSC	*R*	18.86 ± 0.02	(1)
0.227	Xinglong 2.16 m/BFOSC	*V*	19.88 ± 0.06	(1)
0.231	Xinglong 2.16 m/BFOSC	*B*	>21.9	(1)
2.203	Xinglong 2.16 m/BFOSC	*R*	21.26 ± 0.08	(1)
2.227	Xinglong 2.16 m/BFOSC	*I*	19.95 ± 0.03	(1)
2.255	Xinglong 2.16 m/BFOSC	*V*	>22.0	(1)
4.219	Xinglong 2.16 m/BFOSC	*I*	20.80 ± 0.04	(1)
4.255	Xinglong 2.16 m/BFOSC	*R*	22.28 ± 0.13	(1)
7.221	Xinglong 2.16 m/BFOSC	*I*	21.3 ± 0.1	(1)
0.327	NEXT	*r*	19.30 ± 0.06	(1)
0.436	NEXT	*g*	>21.6	(1)
0.454	NEXT	*r*	19.52 ± 0.06	(1)
0.474	NEXT	*i*	18.22 ± 0.03	(1)
0.493	NEXT	*z*	17.77 ± 0.08	(1)
1.390	NEXT	*i*	19.53 ± 0.08	(1)
1.410	NEXT	*z*	19.32 ± 0.17	(1)
1.443	NEXT	*r*	21.12 ± 0.17	(1)
2.415	NEXT	*i*	20.24 ± 0.16	(1)
2.396	NEXT	*r*	21.40 ± 0.25	(1)
2.415	NEXT	*i*	20.24 ± 0.16	(1)
2.435	NEXT	*z*	19.84 ± 0.22	(1)
0.544	CAHA 2.2 m/CAFOS	*i*	18.30 ± 0.03	(1)
0.546	CAHA 2.2 m/CAFOS	*i*	18.28 ± 0.03	(1)
0.548	CAHA 2.2 m/CAFOS	*i*	18.35 ± 0.03	(1)
0.549	CAHA 2.2 m/CAFOS	*r*	19.77 ± 0.06	(1)
0.551	CAHA 2.2 m/CAFOS	*r*	19.80 ± 0.06	(1)
0.552	CAHA 2.2 m/CAFOS	*r*	19.71 ± 0.05	(1)
0.556	CAHA 2.2 m/CAFOS	*g*	22.19 ± 0.13	(1)
0.592	CAHA 2.2 m/CAFOS	*r*	19.84 ± 0.06	(1)
0.596	CAHA 2.2 m/CAFOS	*r*	19.79 ± 0.04	(1)
0.598	CAHA 2.2 m/CAFOS	*r*	19.85 ± 0.04	(1)
0.600	CAHA 2.2 m/CAFOS	*r*	19.83 ± 0.04	(1)
0.601	CAHA 2.2 m/CAFOS	*i*	18.38 ± 0.02	(1)
0.604	CAHA 2.2 m/CAFOS	*i*	18.44 ± 0.02	(1)
0.605	CAHA 2.2 m/CAFOS	*i*	18.40 ± 0.02	(1)
0.607	CAHA 2.2 m/CAFOS	*i*	18.43 ± 0.03	(1)
0.609	CAHA 2.2 m/CAFOS	*i*	18.39 ± 0.03	(1)
0.611	CAHA 2.2 m/CAFOS	*i*	18.42 ± 0.03	(1)
1.545	CAHA 2.2 m/CAFOS	*r*	21.02 ± 0.05	(1)
1.556	CAHA 2.2 m/CAFOS	*i*	19.59 ± 0.03	(1)
2.556	CAHA 2.2 m/CAFOS	*i*	20.34 ± 0.04	(1)
6.597	CAHA 2.2 m/CAFOS	*r*	>22.7	(1)
6.611	CAHA 2.2 m/CAFOS	*i*	21.61 ± 0.17	(1)
0.658	NOT/ALFOSC	*r*	19.87 ± 0.01	(1)
5.687	NOT/ALFOSC	*r*	22.74 ± 0.13	(1)
5.699	NOT/ALFOSC	*i*	21.37 ± 0.09	(1)
9.644	NOT/ALFOSC	*i*	22.15 ± 0.09	(1)
0.710	Tautenburg 1.34 m/TAUKAM	*r*	19.86 ± 0.13	(1)
1.666	Tautenburg 1.34 m/TAUKAM	*g*	>20.96	(1)
5.545	Tautenburg 1.34 m/TAUKAM	*z*	20.78 ± 0.16	(1)
5.565	Tautenburg 1.34 m/TAUKAM	*i*	21.37 ± 0.10	(1)
5.599	Tautenburg 1.34 m/TAUKAM	*r*	22.81 ± 0.24	(1)
5.634	Tautenburg 1.34 m/TAUKAM	*g*	>23.8	(1)
1.67	TNG/NICS	*J*	19.21 ± 0.07	(1)
1.67	TNG/NICS	*H*	18.89 ± 0.06	(1)
1.67	TNG/NICS	*Ks*	18.65 ± 0.07	(1)
4.63	TNG/NICS	*J*	20.61 ± 0.10	(1)
4.63	TNG/NICS	*Ks*	19.57 ± 0.10	(1)
9.61	TNG/NICS	*J*	21.56 ± 0.25	(1)
6.604	GTC/EMIR	*Y*	22.40 ± 0.16	(1)
6.614	GTC/EMIR	*J*	21.46 ± 0.14	(1)
6.623	GTC/EMIR	*H*	20.89 ± 0.12	(1)
6.637	GTC/EMIR	*Ks*	20.73 ± 0.08	(1)
36.97	HST/WFC3	F775W	26.61 ± 0.08	(1)
37.04	HST/WFC3	F125W	25.54 ± 0.05	(1)
0.624	LT/IO:O	*g*	21.97 ± 0.1	(2)
0.625	LT/IO:O	*R*	19.84 ± 0.03	(2)
0.627	LT/IO:O	*I*	18.48 ± 0.03	(2)
0.629	LT/IO:O	*z*	18.20 ± 0.03	(2)
0.675	LT/IO:O	*g*	22.21 ± 0.13	(2)
0.677	LT/IO:O	*r*	19.92 ± 0.03	(2)
0.678	LT/IO:O	*I*	18.58 ± 0.03	(2)
0.680	LT/IO:O	*z*	18.27 ± 0.03	(2)
1.592	LT/IO:O	*r*	21.17 ± 0.06	(3)
1.596	LT/IO:O	*i*	19.70 ± 0.04	(3)
1.599	LT/IO:O	*z*	19.48 ± 0.05	(3)
2.707	LT/IO:O	*z*	19.97 ± 0.12	(3)
2.712	LT/IO:O	*i*	20.39 ± 0.08	(3)
2.715	LT/IO:O	*r*	21.58 ± 0.17	(3)
3.693	LT/IO:O	*z*	20.61 ± 0.12	(3)
3.698	LT/IO:O	*r*	22.31 ± 0.17	(3)
3.703	LT/IO:O	*i*	20.89 ± 0.09	(3)
4.596	LT/IO:O	*z*	20.63 ± 0.11	(3)
4.601	LT/IO:O	*i*	21.25 ± 0.11	(3)
4.605	LT/IO:O	*r*	23.13 ± 0.34	(3)
6.702	LT/IO:O	*i*	21.34 ± 0.19	(3)

Note. ΔT is the exposure median time after the BAT trigger. Magnitudes in the AB system are *not* corrected for Galactic extinction, which is $E(B-V) = 0.05$ (Schlafly & Finkbeiner 2011). References: (1) this work, (2) Perley (2022a), (3) Perley (2022b).

Many ground-based observatories contributed to the afterglow observations of the burst, and the results are available in the GRB Coordinates Network (GCN).[25] In our following analysis, we take into account the observations reported by the Liverpool Telescope team, as the data are calibrated with the SDSS catalog and reported in AB magnitudes (Perley 2022a, 2022b).

To compare the afterglow of GRB 220101A with a sample of historical GRB optical lightcurves, we shifted (in time and flux) the afterglow to redshift $z = 1$. According to the difference between the observed flux of the *R* band and the modeled *R*-band flux obtained from Section 3.4, we corrected the affected flux to the pseudo-real magnitude by adding $\Delta m = -1.1$ magnitude. In order to show the lightcurve of the whole period, we modified the lightcurve of the *white*, *r*, and *J* bands to the *R* band. The final whole period lightcurve compared with the historic sample is shown in Figure 3. It is clear that the optical afterglow of GRB 220101A is one of the most luminous ones ever observed, comparable to the high-redshift burst GRB 050904 (Zou et al. 2006; Kann et al. 2007)

[25] https://gcn.gsfc.nasa.gov/gcn3_archive.html

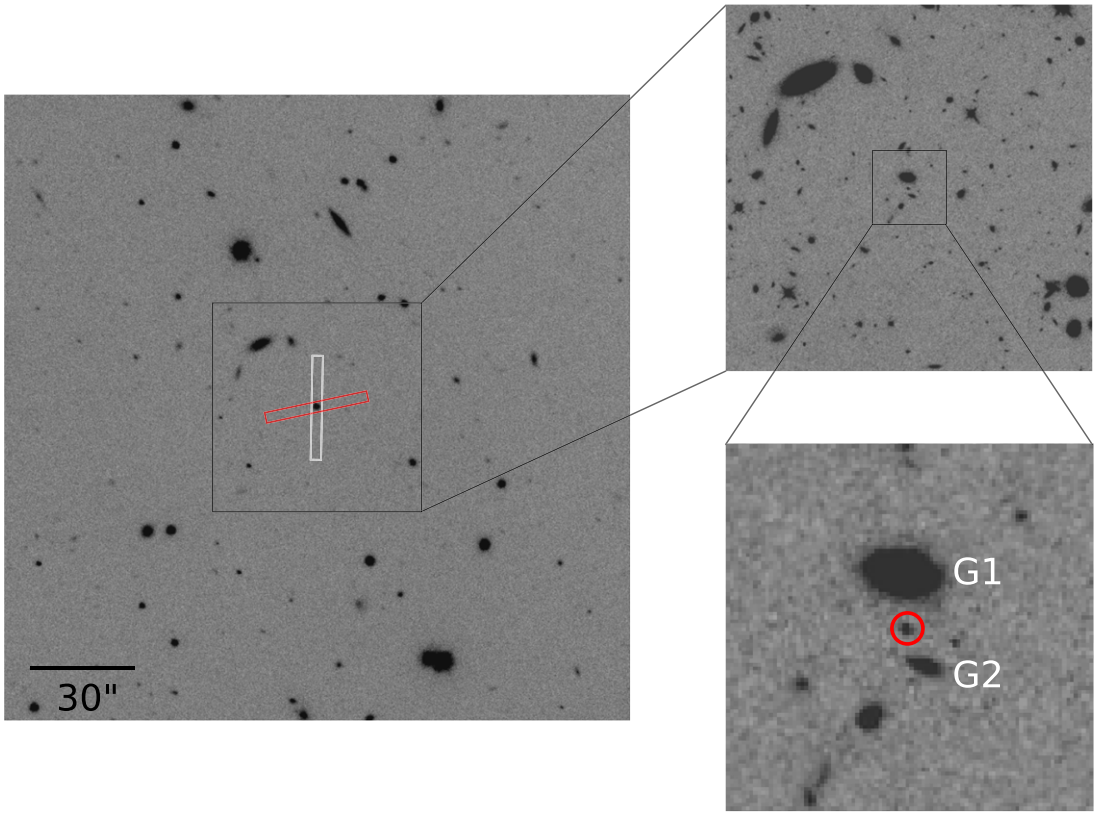

Figure 1. The *r*-band field view of GRB 220101A obtained by ALFOSC on the first night (left) and the later-time observations with HST in the F125W filter (top and bottom right). The slit direction of ALFOSC and BFOSC is also shown in the left panel of the figure as red and white rectangles, respectively. In the zoomed view of HST, the burst is circled in red and two galaxies are nearby, named G1 (R.A., decl. (J2000) = 00:05:24.83, +31:46:09.91) and G2 (R.A., decl. (J2000) = 00:05:24.77, +31:46:06.86). The burst offset to G1 and G2 is $1\farcs83 \pm 0\farcs02$ and $1\farcs38 \pm 0\farcs02$, respectively, corresponding to 12.2 ± 0.1 and 9.2 ± 0.1 kpc at a common redshift of 4.615 ± 0.001. North is up and east is to the left.

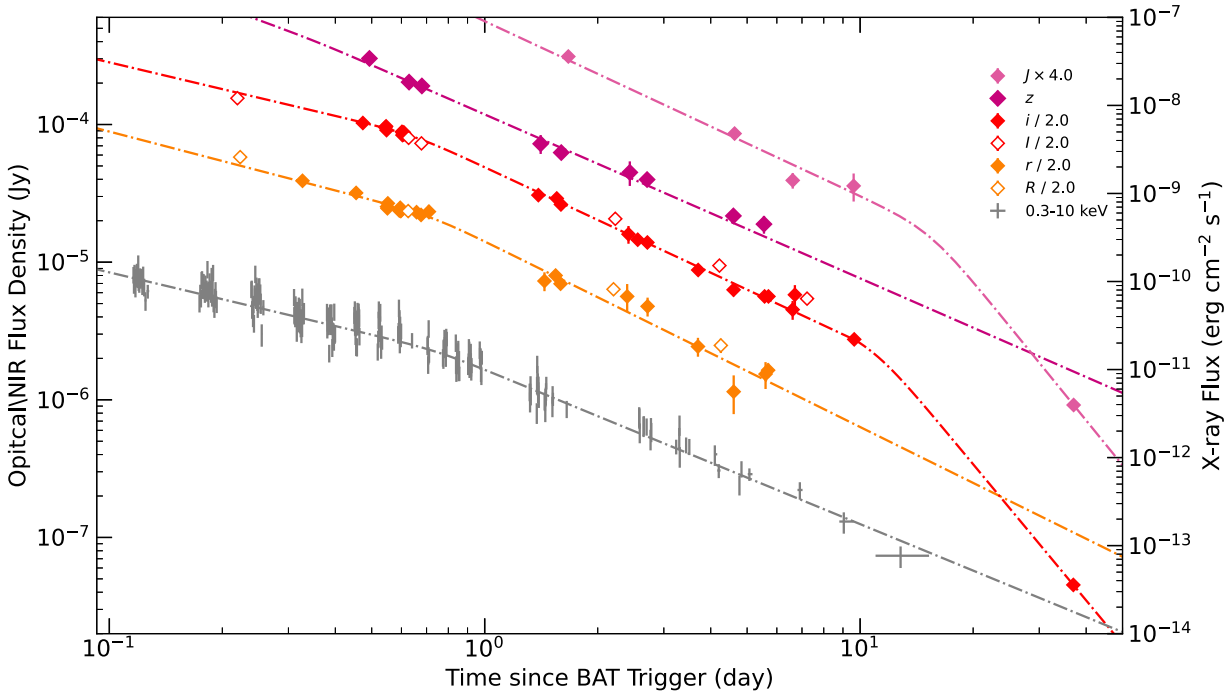

Figure 2. The multiband lightcurves of GRB 220101A. The detection points in the figure are in the AB system and have been corrected for Galactic extinction, which is $E(B-V) = 0.05$ (Schlafly & Finkbeiner 2011). The last *i*- and *J*-band points correspond to the HST F775W and F125W detections, respectively. The fits of different bands are represented by dashed lines of corresponding colors, and the fitting results are listed in Table 3.

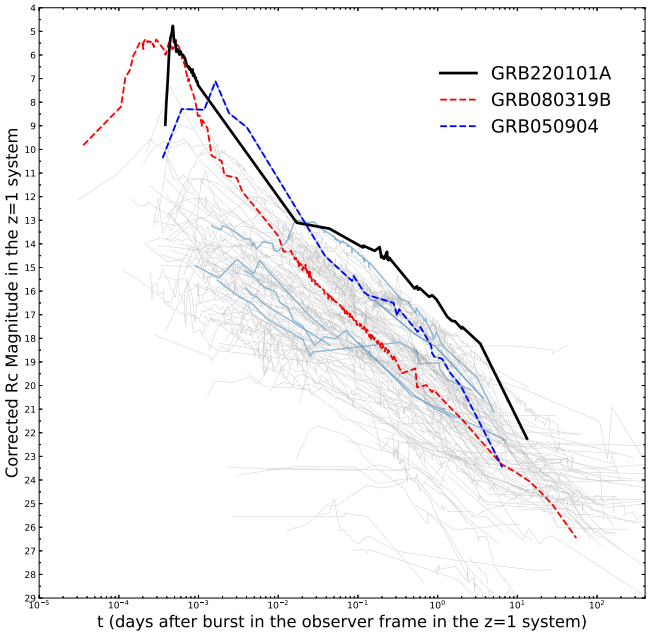

Figure 3. "Kann plot" comparing a large sample of GRB optical afterglow lightcurves shifted in time and flux to a common redshift of $z = 1$ following Kann et al. (2010). The gray background are historical data of other GRB lightcurves. GRB 220101A is shown as a black solid line, which lies at the top of the distribution in terms of luminosity. The bursts with redshifts larger than 4 are colored in light blue.

and the naked-eye burst GRB 080319B (Bloom et al. 2009), and exceeding even this well-known energetic event in some aspects.

2.3. Spectroscopy

After obtaining the multiband (*BVRI*) photometry results from BFOSC, we noticed a very significant drop between the *B* and *V* bands, with $m_B - m_V > 2$. Subsequently, we realized this could be a relatively high-redshift signal with $z > 3$ if the drop is due to absorption of Lyα. Taking into account the current magnitude and potential high redshift, we immediately acquired 3×1800 s exposure spectroscopic observations approximately 0.3 day after the burst. Using the $2\farcs3$ slit, the order-sorter filter 385LP, and the G4 grating with 1×1 binning, we luckily got a spectral coverage of 3800–9000 Å with the three exposures. We processed the spectra using the standard IRAF data reduction techniques and performed flux calibration with the standard star HD 19445 (Oke & Gunn 1983) observed on the same night with the same instrument setup. The reduced BFOSC spectrum is shown in the top panel of Figure 4. The significant Lyα drop, S II, Si II, the mixed C II, and the mixed C IV double lines led to us to calculate a 4.61 redshift for the burst, which confirmed our previous hypothesis. The spectral redshift confirms this is the most distant gamma-ray burst ever identified by BFOSC, which is mounted on the Xinglong 2.16 m telescope.

We used ALFOSC mounted on the NOT to obtain more detailed spectral information about 0.6 days after the burst. Using a $1\farcs3$ slit and a volume phase holographic grism with a fixed order-blocker filter called OG550 resulted in a wavelength range of 5650 Å to 10150 Å. We used 2×2 binning to improve the signal-to-noise ratio. The extracted spectrum is displayed in the bottom panel of Figure 4 and was obtained using the standard IRAF spectrum processing tasks. The identified metal lines are also marked in Figure 4 and listed in Table 2 along with the measured equivalent widths (EW). From the lines including Lyα, N V, S II, Si II, C II, C II*, and C IV, we determined a redshift of $z = 4.615 \pm 0.001$, which is in full agreement with the BFOSC redshift.

The redshift of the burst was finally determined to be 4.615 ± 0.001. We also fit the profile of Lyα, which is shown in Figure 5 with a fit result of $\log (N_{\rm HI}/cm^{-2}) = 21.55 \pm 0.08$. In Figure 6, we compare the column density of $N_{\rm HI}$ with that of other $z > 4$ bursts. The neutral hydrogen column density in the GRB host galaxy along the line of sight is well in line with the average value in the density sample, for which the redshifts are between 4 and 5.

3. Multiband Analysis and External Shock Modeling

3.1. Mirror Feature in Prompt Phase

Hakkila (2021) studied a sample of BATSE GRBs and found that 86% of the GRB pulses can be characterized by a smooth, single-peaked component coupled with a temporally symmetrical residual structure. Following their approach, we analyzed the GBM data of GRB 220101A and found that prompt emission of the burst is a typical "time symmetric" pulse. The monotonic component is fitted by Gaussian model and the fitting result is shown in Figure 7. The residual structure obtained by subtracting the monotonic component from the data is highly symmetric. There are two main pulses: one is a typical pulse with a fast rise and exponential decay (FRED), and the other is just its time symmetric form, with the symmetric time $t_{0;\rm mirror} = 100.7$ s and stretching parameter $s_{\rm mirror} = 0.75$. The uncertainty of the stretching parameter estimated by resampling the data shows $\sigma_{s,\rm mirror} = 0.18$ (Andrae 2010), satisfying the criterion $\sigma_{s,\rm mirror} < 0.4$. This feature may bring new implications for understanding the production of gamma-ray bursts. Kinematic behaviors might explain this "mirrored" wavelike structure. Hakkila et al. (2018) assumed that each GRB pulse involves a single impactor interacting with an independent medium. When the impactor is reflected after passing through the cloud or the impactor goes straight through a symmetrical structure, the time-reversed and stretched components can be produced. The transition of the impactor wave between subliminal and superluminal velocities can also produce this component (Hakkila & Nemiroff 2019). The radiation produced at the superluminal part is exactly the time-reversed version of the subliminal part. However, the exact reason for such a mirror feature is still a mystery.

3.2. Temporal Analysis

The obtained lightcurve is from ~0.2 day to ~30 days, from the optical to near-infrared, including *g, r, i, z, R, I, J, H, K* bands. We first made a rough analysis of the data before fitting and found that our optical afterglow can be simply divided into three stages: the shallow decay phase, followed the normal decay phase, and then the late decay phase. The lightcurves with rich detection points (*r*, *i*, *z*, and *J*)were selected for decay index fitting. For the band without break, *z*, the simple power-law (SPL) function $F \propto t^{-\alpha}$ is used. The bands with one break, *r* and *J*, are fit with the smooth broken power-law (BPL)

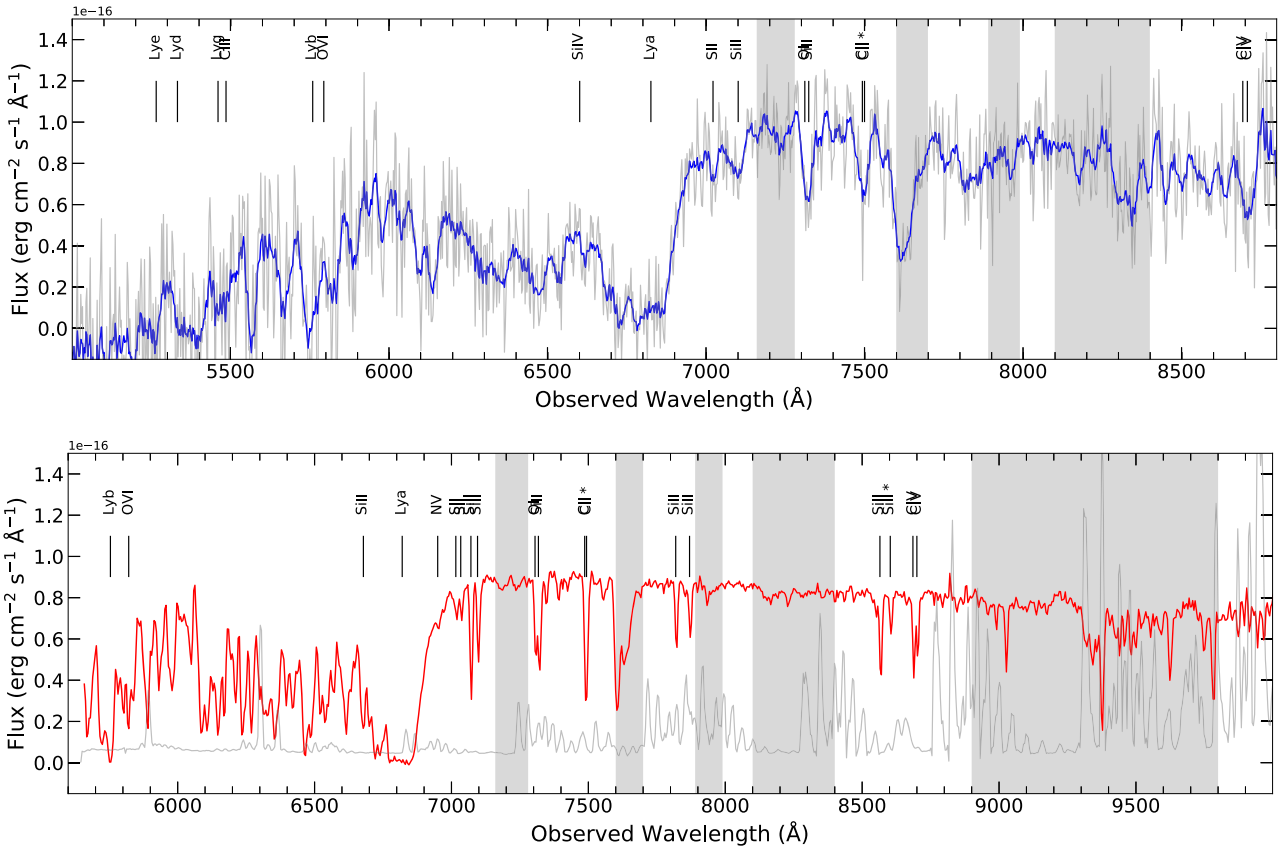

Figure 4. The spectra of the afterglow obtained by Xinglong 2.16 m/BFOSC and NOT/ALFOSC, respectively. Top panel: the spectrum obtained by BFOSC. The gray line is the raw spectrum and the blue is smoothed for display purposes. Bottom panel: the spectrum obtained by ALFOSC. The gray line is the background sky spectrum and the red line is the raw spectrum of the burst. In the both panels, the identified metal absorption lines are indicated with vertical lines in the figure, and the possible lines at the left of Lyα are also marked. The gray vertical bands indicate the telluric features in both panels.

Table 2
List of Spectral Features and Their Equivalent Widths

λ_{obs}(Å)	Feature(Å)	z	EW_{obs}(Å)
	ALFOSC		
6952.5	N V $\lambda\lambda$1238.2	4.615	0.64 ± 0.26
7019.76	S II $\lambda\lambda$1250.0	4.616	0.91 ± 0.48
7037.41	S II $\lambda\lambda$1253.2	4.616	0.91 ± 0.48
7072.43	Si II $\lambda\lambda$1259.8	4.614	4.87 ± 1.32
7098.67	Si II $\lambda\lambda$1264.2	4.615	3.68 ± 1.46
7315.86	O I/Si II $\lambda\lambda$1302.7	4.616	9.01 ± 1.84
7492.53	C II/C II*$\lambda\lambda$1334.5	4.614	8.31 ± 1.58
7821.88	Si II $\lambda\lambda$1393.2	4.614	3.16 ± 1.28
7872.56	Si II $\lambda\lambda$1402.2	4.614	2.55 ± 1.28
8567.87	Si II $\lambda\lambda$1526.1	4.614	6.83 ± 1.53
8605.41	Si II*$\lambda\lambda$1532.9	4.614	3.3 ± 1.4
8694.91	C IV/C IV $\lambda\lambda$1548.9	4.614	10.02 ± 1.76

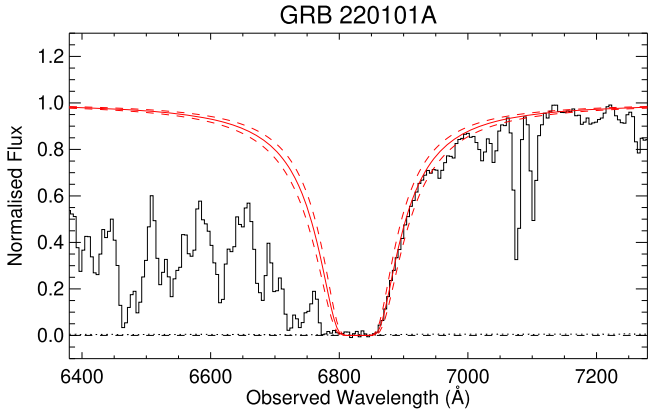

Figure 5. The best fit of the Lyα break. The neutral hydrogen column density is log $(N_{HI}/cm^{-2}) = 21.55 \pm 0.08$ at a redshift $z = 4.615$.

function,

$$F = F_0\left(\left(\frac{t}{t_b}\right)^{\omega\alpha_1} + \left(\frac{t}{t_b}\right)^{\omega\alpha_2}\right)^{-1/\omega} \quad (1)$$

where α_1 and α_2 are the decay index before and after the break time t_b, and ω is the sharpness of the break, which is fixed to 1 in our fitting. For the band with two breaks, i, the BPL function is used for the first and second break, respectively, and the $\alpha_{2,i}$ obtained from the first fitting is fixed in the second fitting. The X-ray lightcurve can be divided into two stages, the early and late phases, which are also fitted with the BPL function. All the fitting results above are listed in Table 3.

3.3. Afterglow Spectral Energy Distribution Analysis

A spectral energy distribution (SED) analysis enables a deeper understanding of the afterglow evolution. In this study, we performed an SED analysis on four epochs of XRT data (0.3–10 keV) obtained from the online repository combined

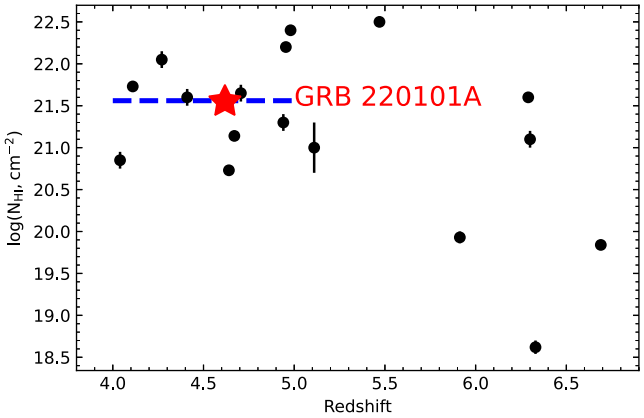

Figure 6. The H I column density of $z > 4$ GRBs. The blue dashed line represents the average density of those with a redshift of between 4 and 5. The data points are collected from Thöne et al. (2013), Chornock et al. (2014), Laskar et al. (2018), and Saccardi et al. (2023).

with optical data,[26] denoted as Epochs 1–4. The detailed information of each epoch and the optical data is listed in Table 4. We utilized the Xspec package (version 12.12) to fit the data of these epochs with the power-law model, accounting for the dust extinction of the host galaxy (Small Magellanic Cloud with $R_V = 2.93$; Pei 1992) and the photoelectric absorption of the host galaxy and the Milky Way. To enhance the signal-to-noise ratio, the X-ray data were rebinned using the "grppha" tool to ensure at least 20 photons per bin. The Galactic column density of hydrogen ($N_{\rm H,Gal} = 6.29 \times 10^{20}$ cm^{-2}) was obtained from the Calculate Galactic NH tool.[27]

Given the wealth of optical data available for Epoch 3, we conducted SED fitting for this epoch as an initial step. Our analysis revealed that the extinction caused by the host galaxy can be disregarded, as the color excess ($E(B-V)$) is only 0.02. Therefore, we set the value of $E(B-V)$ to zero for our fitting. Our results demonstrate that a single power law suffices to accurately fit all epochs, which suggests that the optical and X-ray emissions occupy the same spectral regime. The fit lines are illustrated in Figure 8, and the results are presented in Table 4.

3.4. External Shock Modeling

In the standard external shock fireball model, the optical, near-infrared, and X-ray emissions from afterglows can be understood to come from the synchrotron emission that results from the interaction between a relativistic jet and a constant (interstellar medium; ISM) or wind-type external medium (Rees & Meszaros 1992; Mészáros & Rees 1997; Sari et al. 1998; Zhang 2018). Electrons are believed to be accelerated at the shock front into a power-law distribution $N(\gamma_{\rm e}) \propto \gamma_{\rm e}^{-p}$. A fraction $\epsilon_{\rm e}$ of the shock energy is distributed into electrons, and a fraction $\epsilon_{\rm B}$ is in the magnetic field generated behind the shock. Accounting for the radiative cooling and the continuous injection of new accelerated electrons at the shock front, one expects a broken power law energy spectrum for them, which leads to a multisegment broken power law radiation spectrum separated by three characteristic frequencies at any epoch: the synchrotron cooling frequency $\nu_{\rm c}$, the synchrotron frequency $\nu_{\rm m}$ defined by the minimum electron Lorentz factor, and the synchrotron self-absorption frequency $\nu_{\rm a}$ (below which the synchrotron photons are self absorbed; see Gao et al. 2013 and Zhang 2018 for a review). Usually, the self-absorption frequency does not affect the X-ray and optical data at early epochs, and it mainly affects the low-frequency observations of afterglows.

Based on the afterglow SED analysis, the spectral index $\beta_{\rm OX} \sim 0.6$ in the optical to X-ray bands (see Figure 8 and Table 4). For the time period we are interested in (∼days), the jet might enter the deceleration phase. The spectrum is likely in the slow-cooling regime, and the optical and X-ray emissions may lie between $\nu_{\rm m}$ and $\nu_{\rm c}$, i.e., $\nu_{\rm m} < \nu < \nu_{\rm c}$. In this case, $\beta_{\rm OX} = (p-1)/2$ is expected. Therefore, we have $p \sim 2.2$ by comparing with the observed SED. From the closure relation analysis for the ISM and wind cases, the temporal decay indices α in a self-similar deceleration phase for $\nu_{\rm a} < \nu_{\rm m} < \nu < \nu_{\rm c}$ and $p > 2$ are (Gao et al. 2013; see Table 13 therein)

$$F_\nu \propto \begin{cases} t^{-\frac{3(p-1)}{4}}, & \text{ISM}, \\ t^{-\frac{3p-1}{4}}, & \text{Wind}. \end{cases} \quad (2)$$

This corresponds to $\alpha_{\rm ISM} = 3(p-1)/4 = 0.9$ and $\alpha_{\rm Wind} = (3p-1)/4 = 1.4$ using $p = 2.2$. Comparing with the temporal analysis of the optical and X-ray afterglow lightcurves (see Figure 2 and Table 3), the observational data ($\alpha < 1.0$) favors the ISM model.

We thus assumed a constant external medium (ISM) and performed a multiband fit to GRB 220101A afterglow data using the public Python package *afterglowpy*, which is an open-source numerical and analytic modeling tool to calculate the synchrotron lightcurve and spectrum from an external shock (Ryan et al. 2020). Such multiband modeling is helpful in constraining the afterglow physical parameters. The model parameters and associated errors are constrained during multiband fitting using the Python package *emcee* (Foreman-Mackey et al. 2013).

Structured jet models (such as top-hat, Gaussian, power law, etc.) are involved in *afterglowpy* to produce the lightcurves. In this paper, we used the top-hat jet-type structure in the modeling of GRB 220101A. Five free parameters were considered: the isotropic kinetic energy $E_{\rm K,iso}$, the half-width of the jet core $\theta_{\rm C}$, the number density of the ISM n_1, the electron distribution power-law index p, and the thermal energy fraction in electrons $\epsilon_{\rm e}$ and in magnetic field $\epsilon_{\rm B}$. The viewing angle $\theta_{\rm O}$ is fixed to 0 in the fit. The r and R bands of the burst are affected by the absorption of Lyα break and the forest; therefore we excluded these two bands in our model fitting.

We used the top-hat jet model and performed a parameter search with 30 walkers over 15,000 iterations, discarding the first 7500 as burn-in steps. The prior type and range for each model parameter are presented in Table 5, including $E_{\rm K,iso} = 3.7^{+0.5}_{-0.2} \times 10^{54}$ erg, $\theta_{\rm C} = 3.4^{+0.6}_{-0.6}$ deg, $n_0 = 0.10^{+0.05}_{-0.05}$ cm^{-3}, $p = 2.44^{+0.01}_{-0.01}$, $\epsilon_{\rm e} = 0.31^{+0.01}_{-0.03}$, and $\epsilon_{\rm B} = 7.4^{+3.6}_{-1.9} \times 10^{-5}$. The fit model with the multiband lightcurve and the contour plot of the model parameters are displayed in Figures 9 and 10, respectively.

4. Discussion

As shown in Figure 8 and Table 4, the spectral index in the optical to X-ray bands is $\beta_{\rm OX} \sim 0.6$. This suggests an electron

[26] https://www.swift.ac.uk/xrt_spectra/
[27] https://www.swift.ac.uk/analysis/nhtot/

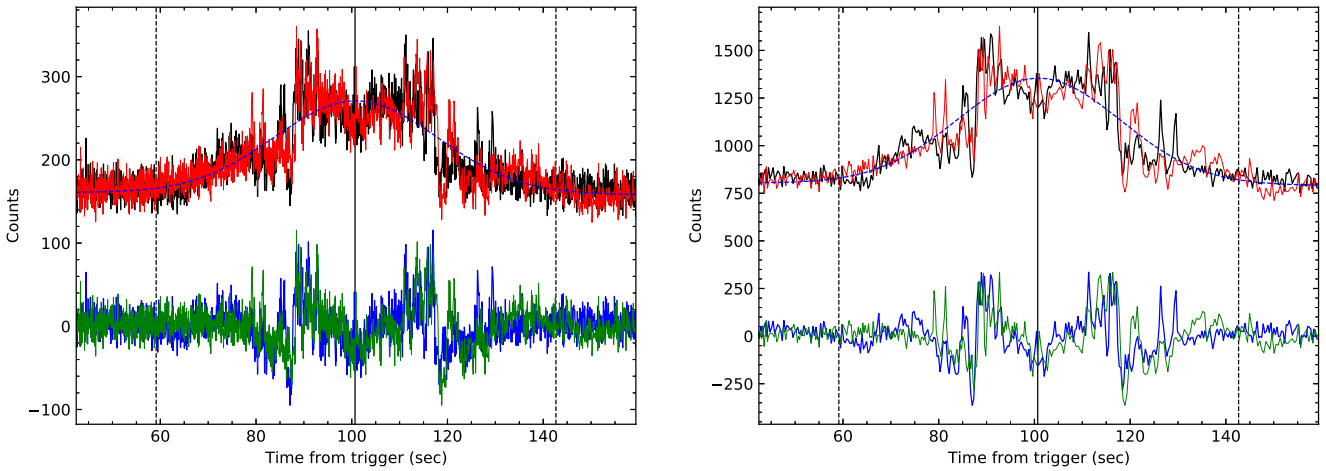

Figure 7. Temporally symmetric model fit to GRB 220101A lightcurve. The left panel shows the 64 ms counts data (black) obtained by NaI detectors n6 and n7 of Fermi/GBM, the fit to the monotonic components (blue dashed line), the time-reversed model (red), the residual (blue), the time-reversed residual (green), the duration window (vertical dashed lines), and the time of reflection (vertical solid line). To display a clearer structure, the same GRB with a time resolution of 320 ms is shown in the right panel.

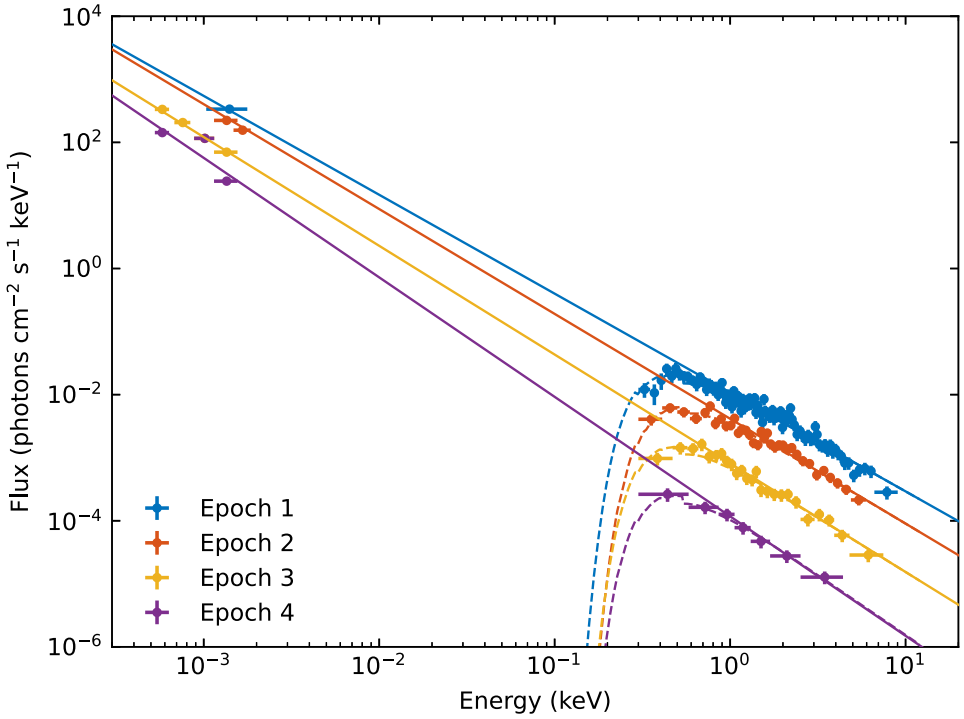

Figure 8. The afterglow SED of GRB 220101A at 20 ks (Epoch 1, blue lines), 60 ks (Epoch 2, orange lines), 150 ks (Epoch 3, yellow lines), and 400 ks (Epoch 4, purple lines) from the optical to X-ray. The optical multiband data are listed in Table 4. The solid and dashed lines are the results of the single power law and the model fit for each epoch.

Table 3
List of Optical, Near-infrared and X-Ray Lightcurve Decay Indices

Band	Model	α	α_1	α_2	t_b (ks)	χ^2/dof
r	BPL	⋯	0.71 ± 0.10	1.35 ± 0.08	63.1 ± 10.4	18.9/17
i	BPL	⋯	0.65 ± 0.19	1.27 ± 0.03	56.4 ± 6.9	15.3/20
	BPL	⋯	1.27 (fixed)	3.3 ± 0.3	947 ± 165	1.3/3
z	SPL	1.19 ± 0.04	⋯	⋯	⋯	8.5/6
J	BPL	⋯	1.27 (fixed)	3.4 ± 0.2	1329 ± 62	6.2/2
X-ray	BPL	⋯	1.01 ± 0.04	1.75 ± 0.05	64.9 ± 6.5	390.3/275

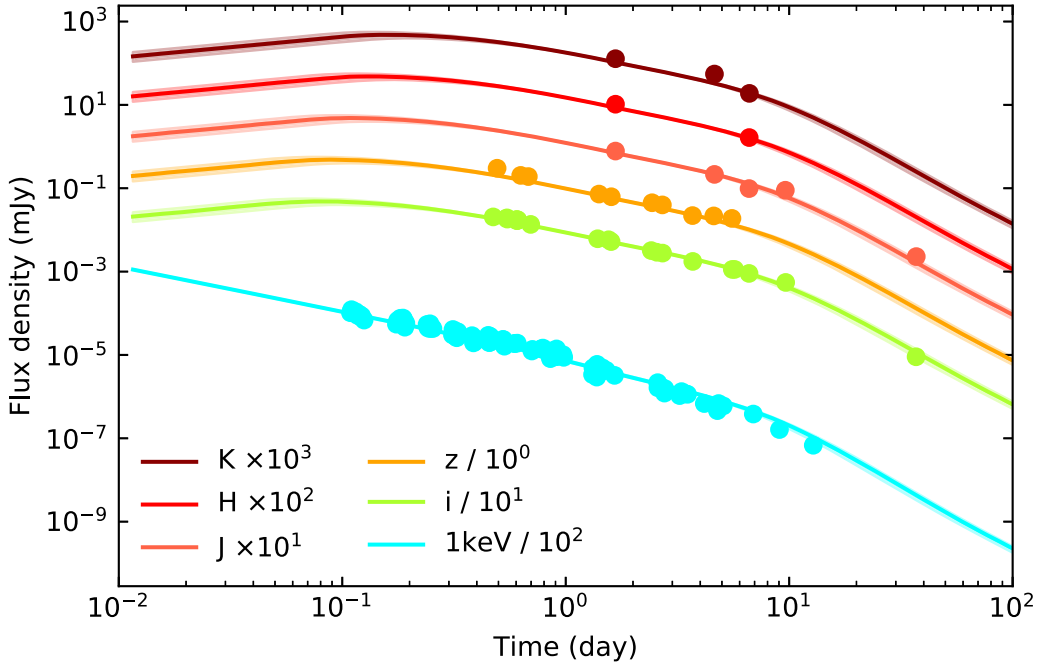

Figure 9. Optical, near-infrared, and X-ray data of GRB 220101A along with the best-fit afterglow modeling. The shaded region is the 2σ error region. X-ray flux density is converted from 0.3 to 10 keV to 1 keV following Gehrels et al. (2008).

Table 4
SED Data at Different Epochs with the Best-fit Indexes

Filter	Epoch 1 (20 ks)	Epoch 2 (54 ks)	Epoch 3 (140 ks)	Epoch 4 (400 ks)
B	>21.7	...	...	...
V	19.72 ± 0.06	...	...	...
R	18.74 ± 0.02	...	...	...
I	17.67 ± 0.01	...	...	...
g	...	21.78 ± 0.10	...	...
r	...	19.74 ± 0.01	21.04 ± 0.06	...
i	...	18.32 ± 0.03	19.60 ± 0.04	21.15 ± 0.11
z	...	18.13 ± 0.03	19.41 ± 0.05	20.56 ± 0.11
J	...	...	19.17 ± 0.07	20.57 ± 0.10
H	...	...	18.86 ± 0.06	...
Ks	...	...	18.63 ± 0.07	19.55 ± 0.10
Γ_1	1.57 ± 0.01	1.66 ± 0.01	1.72 ± 0.01	1.84 ± 0.02
$N_{\rm H,host}$ ($\rm cm^{-2}$)	$(1.8 \pm 3.8) \times 10^{21}$	$(1.7 \pm 0.6) \times 10^{22}$	$(9.1 \pm 7.0) \times 10^{21}$	$\sim 1.2 \times 10^{22}$
χ^2/d.o.f.	$86.8/89 = 0.98$	$34.1/34 = 1.00$	$22.4/26 = 0.86$	$19.7/7 = 2.81$
Γ_1	1.56 ± 0.01	1.66 ± 0.01	1.71 ± 0.01	1.80 ± 0.02
$\Gamma_2 = \Gamma_1 + 0.5$	2.06	2.16	2.21	2.30
E_b (keV)	3.2 ± 0.4	4.0 ± 1.0	3.6 ± 1.0	...
$N_{\rm H,host}$ ($\rm cm^{-2}$)	$(4.9 \pm 4.1) \times 10^{21}$	$(1.8 \pm 0.6) \times 10^{22}$	$(1.1 \pm 0.7) \times 10^{22}$	...
χ^2/d.o.f.	$75.3/88 = 0.86$	$32.8/33 = 0.99$	$17.2/22 = 0.78$	$1.23/4 = 0.31$

Note. The photometric data listed here are corrected for Galactic extinction.

Table 5
Model Input Parameters, Prior Type, Prior Range, and Best-fit Values for GRB 220101A

Parameters	Prior Type	Prior Range	Best Fit
$E_{\rm K,iso}$ (erg)	log flat	10^{52}–6×10^{56}	3.5×10^{54}
$\theta_{\rm C}$ (rad)	flat	0–0.2	0.06
n_0 ($\rm cm^{-3}$)	log flat	10^{-6}–10^{5}	0.15
p	flat	2.3–2.7	2.44
$\epsilon_{\rm e}$	log flat	10^{-6}–0.33	3.3×10^{-1}
$\epsilon_{\rm B}$	log flat	10^{-6}–0.33	5.9×10^{-5}

energy distribution index of $p \sim 2.2$, which is roughly consistent with our fit result, $p = 2.44^{+0.01}_{-0.01}$, obtained with *afterglowpy*.

After the deceleration time, the jet approaches the Blandford & McKee (1976) self-similar evolution

$$\Gamma(t) \simeq \left(\frac{17E_{\rm K,iso}}{1024\pi n_{\rm l} m_{\rm p} c^5 t^3}\right)^{1/8}, \quad R(t) \simeq \left(\frac{17E_{\rm K,iso} t}{4\pi n_{\rm l} m_{\rm p} c}\right)^{1/4}. \quad (3)$$

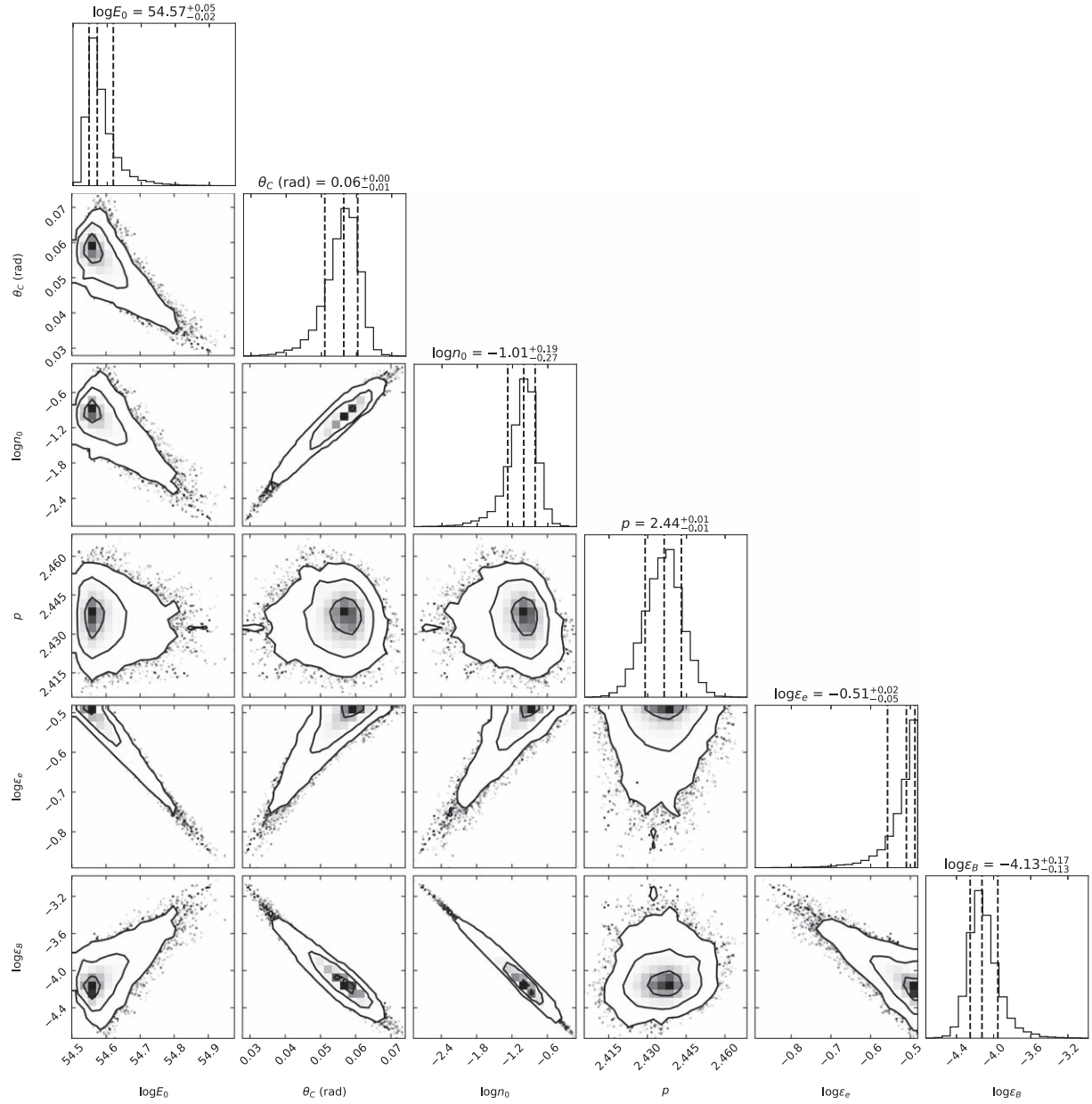

Figure 10. Posterior distribution and parameter constraints obtained using multiband afterglow modeling of GRB 220101A with *afterglowpy*. The median values with the 1σ error regions are also shown in the one-dimensional probability distribution.

Later, the ejecta are decelerated to the post-jet-break phase at the time (Lei et al. 2016; Zhu et al. 2023)

$$t_{\rm j} \simeq 0.6{\rm day}\left(\frac{\theta_{\rm C}}{0.1{\rm rad}}\right)^{8/3}\left(\frac{E_{\rm K,iso}}{10^{53}{\rm erg}}\right)^{1/3} n_1^{-1/3}, \quad (4)$$

when the $1/\Gamma$ cone becomes larger than $\theta_{\rm C}$.

As shown in Table 3, just after the shallow decay phase, a break appears in the optical and X-ray at $\sim 6\times10^5$ s. The change of temporal indices $\Delta\alpha \sim 0.7$, which is consistent with the prediction ($\Delta\alpha = 0.75$) from the standard external shock model (Mészáros & Rees 1999; Gao et al. 2013; Zhang 2018). Therefore, this break is likely the jet break. Using this jet break time, we can estimate the opening angle $\theta_{\rm C} \sim 3.^\circ8$ if we insert $E_{\rm K,iso} = 3.5\times10^{54}$ erg, $n_0 = 0.15\,{\rm cm}^{-3}$, and $t_{\rm j} \simeq 6\times10^5/(1+z)$ s into the analytical expression Equation (1). As shown in Table 5, our numerical modeling gives the opening angle $\theta_{\rm C} \sim 3.^\circ4$, which is consistent with this analytical estimation.

From the observations, the isotropic γ-ray energy is $E_{\gamma,\rm iso} \simeq 3\times10^{54}$ erg (Mei et al. 2022). From our modeling, we found the isotropic kinetic jet energy $E_{\rm K,iso} = 3.5\times10^{54}$ erg. Therefore, the total jet energy is $E_{\rm total} = E_{\gamma,\rm iso} + E_{\rm K,iso} \simeq 6.5\times10^{54}$ erg. The opening angle corrected jet energy would be $E_{\rm j} \sim 6\times10^{51}$ erg, which is well below the maximum rotational energy range of 3×10^{52} erg (Lattimer & Prakash 2016) to 7×10^{52} erg (Haensel et al. 2009) for a standard neutron star with mass $M \sim 1.4\,M_\odot$. Therefore, a magnetar central engine model for GRB 220101A cannot be ruled out by the data.

5. Summary

We present our optical and near-infrared observations of the relatively high redshift "New Year's Burst" GRB 220101A. We measure the redshift using the significant metal lines in the optical spectrum obtained by ALFOSC and BFOSC. Combined with our multiband data and the X-ray lightcurve obtained by XRT, we perform a multiband fit with *afterglowpy*. Our conclusions are summarized as follows:

1. The redshift of the burst is taken to be $z = 4.615 \pm 0.001$. The H I column density in the GRB host galaxy along the line of sight is $\log(N_{\rm HI}/{\rm cm}^{-2}) = 21.55 \pm 0.08$.
2. A mirror feature is found in the prompt phase, but its physical origin is unclear.
3. We performed a comparison with a large sample of GRB optical afterglow lightcurves shifted in time and flux to a common redshift of $z = 1$, and it is clear that GRB 220101A is one of the most luminous GRBs ever detected.
4. The standard external shock model can be used to interpret the multiband afterglow data (optical, near-infrared, and X-ray). Based on our observations and modeling, we determined that the total jet energy is $E_{\rm total} = E_{\gamma,{\rm iso}} + E_{\rm K,\ iso} \simeq 6.5 \times 10^{53}$ erg.
5. The breaks at a few 10^5 s in both X-ray and optical bands are roughly consistent with the jet break, revealing an opening angle of $\sim 3.^{\circ}4$. The opening angle corrected jet energy would be $E_{\rm j} \sim 6 \times 10^{51}$ erg.

Acknowledgments

We acknowledge the support of the staff of the Xinglong 2.16 m telescope, NOT, NEXT, CAHA 2.2 m, Tautenburg, TNG, and GTC. The data presented here were obtained in part with ALFOSC, which is provided by the Instituto de Astrofisica de Andalucia (IAA) under a joint agreement with the University of Copenhagen and NOT. This research has made use of the Spanish Virtual Observatory (http://svo.cab.inta-csic.es) supported by the MINECO/FEDER through grant AyA2017-84089.7. This work was also partially supported by the Open Project Program of the Key Laboratory of Optical Astronomy, National Astronomical Observatories, Chinese Academy of Sciences. Based on observations made with the Gran Telescopio Canarias (GTC), installed at the Spanish Observatorio del Roque de los Muchachos of the Instituto de Astrofísica de Canarias, on the island of La Palma, under program ID GTCMULTIPLE2H-21B. This research is based on observations made with the NASA/ESA Hubble Space Telescope obtained from the Space Telescope Science Institute, which is operated by the Association of Universities for Research in Astronomy, Inc., under NASA contract NAS 5-26555. These observations are associated with program 16838. Based on observations made with the NASA/ESA Hubble Space Telescope, and obtained from the Hubble Legacy Archive, which is a collaboration between the Space Telescope Science Institute (STScI/NASA), the Space Telescope European Coordinating Facility (ST-ECF/ESAC/ESA) and the Canadian Astronomy Data Centre (CADC/NRC/CSA). Some of the data presented in this paper were obtained from the Mikulski Archive for Space Telescopes (MAST) at the Space Telescope Science Institute. The specific observations analyzed can be accessed via 10.17909/r9sc-a175. STScI is operated by the Association of Universities for Research in Astronomy, Inc., under NASA contract NAS 5-26555. Support to MAST for these data is provided by the NASA Office of Space Science via grant NAG5-7584 and by other grants and contracts. This work is supported by the National Key R&D Program of China (No. 2020YFC2201400) and the National Natural Science Foundation of China under grant Nos. U2038107 and U1931203. We acknowledge the science research grants from the China Manned Space Project with No. CMS-CSST-2021-A13 and CMS-CSST-2021-B11. W.-H. L. acknowledges support by the science research grants from the China Manned Space Project with No. CMS-CSST-2021-B11. J.P.U.F. acknowledges support from the Carlsberg Foundation. Data resources are supported by the China National Astronomical Data Center (NADC) and Chinese Virtual Observatory (China-VO). The Cosmic Dawn Center (DAWN) is funded by the Danish National Research Foundation under grant No. 140. This work is supported by the Astronomical Big Data Joint Research Center, co-founded by National Astronomical Observatories, Chinese Academy of Sciences, and Alibaba Cloud. We acknowledge the use of public data from the Swift data archive.

Software: Afterglowpy (Ryan et al. 2020), Astrometry.net (Lang et al. 2010), Astropy (Astropy Collaboration et al. 2022), EMCEE (Foreman-Mackey et al. 2013), IRAF (Tody 1986), Matplotlib (Hunter 2007), Numpy (Harris et al. 2020), Photutils (Bradley et al. 2021), PSFEx (Bertin 2011), Python (Van Rossum & Drake 2009), Scipy (Virtanen et al. 2020), Source Extractor (Bertin & Arnouts 1996).

ORCID iDs

Zi-Pei Zhu https://orcid.org/0000-0002-9022-1928
Wei-Hua Lei https://orcid.org/0000-0003-3440-1526
Daniele B. Malesani https://orcid.org/0000-0002-7517-326X
Dong Xu https://orcid.org/0000-0003-3257-9435
José Feliciano Agüí Fernández https://orcid.org/0000-0001-6991-7616
Johan P. U. Fynbo https://orcid.org/0000-0002-8149-8298
Xing Gao https://orcid.org/0000-0002-7292-3109
David Alexander Kann https://orcid.org/0000-0003-2902-3583
Sylvio Klose https://orcid.org/0000-0001-8413-7917
Jin-Zhong Liu https://orcid.org/0000-0002-7420-6744
Massimiliano De Pasquale https://orcid.org/0000-0002-4036-7419
Antonio de Ugarte Postigo https://orcid.org/0000-0001-7717-5085
Bringfried Stecklum https://orcid.org/0000-0001-6091-163X
Christina Thöne https://orcid.org/0000-0002-7978-7648
He Gao https://orcid.org/0000-0002-3100-6558
Shuo Xiao https://orcid.org/0000-0003-2957-2806
Yuan-Chuan Zou https://orcid.org/0000-0002-5400-3261
Li-Ping Xin https://orcid.org/0000-0002-9422-3437

References

Abbott, B. P., Abbott, R., Abbott, T. D., et al. 2017, ApJL, 848, L12
Abolfathi, B., Aguado, D. S., Aguilar, G., et al. 2018, ApJS, 235, 42
Ahumada, T., Singer, L. P., Anand, S., et al. 2021, NatAs, 5, 917
Andrae, R. 2010, arXiv:1009.2755

Arimoto, M., Scotton, L., Longo, F. & Fermi-LAT Collaboration 2022, GCN, 31350, 1
Astropy Collaboration, Price-Whelan, A. M., Lim, P. L., et al. 2022, ApJ, 935, 167
Atteia, J. L., Heussaff, V., Dezalay, J. P., et al. 2017, ApJ, 837, 119
Barthelmy, S. D., Barbier, L. M., Cummings, J. R., et al. 2005, SSRv, 120, 143
Bertin, E. 2011, in ASP Conf. Ser. 442, Astronomical Data Analysis Software and Systems XX, ed. I. N. Evans et al. (San Francisco, CA: ASP), 435
Bertin, E., & Arnouts, S. 1996, A&AS, 117, 393
Blandford, R. D., & McKee, C. F. 1976, PhFl, 19, 1130
Bloom, J. S., Perley, D. A., Li, W., et al. 2009, ApJ, 691, 723
Bradley, L., Sipőcz, B., Robitaille, T., et al. 2021, astropy/photutils: v1.2.0, Zenodo, doi:10.5281/zenodo.5525286
Chornock, R., Berger, E., Fox, D. B., et al. 2014, arXiv:1405.7400
Cucchiara, A., Levan, A. J., Fox, D. B., et al. 2011, ApJ, 736, 7
Della Valle, M., Chincarini, G., Panagia, N., et al. 2006, Natur, 444, 1050
Evans, P. A., Beardmore, A. P., Page, K. L., et al. 2007, A&A, 469, 379
Evans, P. A., Beardmore, A. P., Page, K. L., et al. 2009, MNRAS, 397, 1177
Fan, Z., Wang, H., Jiang, X., et al. 2016, PASP, 128, 115005
Foreman-Mackey, D., Hogg, D. W., Lang, D., & Goodman, J. 2013, PASP, 125, 306
Fryer, C. L., Lien, A. Y., Fruchter, A., et al. 2022, ApJ, 929, 111
Fu, S. Y., Zhu, Z. P., Xu, D., Liu, X., & Jiang, S. Q. 2022, GCN, 31353, 1
Fynbo, J. P. U., de Ugarte Postigo, A., Xu, D., et al. 2022, GCN, 31359, 1
Fynbo, J. P. U., Watson, D., Thöne, C. C., et al. 2006, Natur, 444, 1047
Galama, T. J., Vreeswijk, P. M., van Paradijs, J., et al. 1999, A&AS, 138, 465
Gao, H., Lei, W.-H., Zou, Y.-C., Wu, X.-F., & Zhang, B. 2013, NewAR, 57, 141
Gehrels, N., Barthelmy, S. D., Burrows, D. N., et al. 2008, ApJ, 689, 1161
Gehrels, N., Chincarini, G., Giommi, P., et al. 2004, ApJ, 611, 1005
Gehrels, N., Norris, J. P., Barthelmy, S. D., et al. 2006, Natur, 444, 1044
Gupta, R., Pandey, S. B., Kumar, A., et al. 2022, JApA, 43, 82
Haensel, P., Zdunik, J. L., Bejger, M., & Lattimer, J. M. 2009, A&A, 502, 605
Hakkila, J. 2021, ApJ, 919, 37
Hakkila, J., Lesage, S., McAfee, S., et al. 2018, ApJ, 863, 77
Hakkila, J., & Nemiroff, R. 2019, ApJ, 883, 70
Harris, C. R., Millman, K. J., van der Walt, S. J., et al. 2020, Natur, 585, 357
Hunter, J. D. 2007, CSE, 9, 90
Jin, Z.-P., Zhou, H., Wang, Y., et al. 2023, arXiv:2301.02407
Kann, D. A., Klose, S., Zhang, B., et al. 2010, ApJ, 720, 1513
Kann, D. A., Masetti, N., & Klose, S. 2007, AJ, 133, 1187
Kouveliotou, C., Meegan, C. A., Fishman, G. J., et al. 1993, ApJL, 413, L101
Kuin, N. P. M., Tohuvavohu, A. & Swift/UVOT Team 2022, GCN, 31351, 1
Lamb, D. Q., & Reichart, D. E. 2000, ApJ, 536, 1
Lang, D., Hogg, D. W., Mierle, K., Blanton, M., & Roweis, S. 2010, AJ, 139, 1782
Laskar, T., Berger, E., Chornock, R., et al. 2018, ApJ, 858, 65
Lattimer, J. M., & Prakash, M. 2016, PhR, 621, 127
Lei, W.-H., Yuan, Q., Zhang, B., & Wang, D. 2016, ApJ, 816, 20
Lesage, S., Meegan, C. & Fermi Gamma-ray Burst Monitor Team 2022, GCN, 31360, 1
Markwardt, C. B., Barthelmy, S. D., Krimm, H. A., et al. 2022, GCN, 31369, 1
Mei, A., Oganesyan, G., Tsvetkova, A., et al. 2022, ApJ, 941, 82
Mészáros, P., & Rees, M. J. 1997, ApJ, 476, 232
Mészáros, P., & Rees, M. J. 1999, MNRAS, 306, L39
Oke, J. B., & Gunn, J. E. 1983, ApJ, 266, 713
Osborne, J. P., Beardmore, A. P., Evans, P. A., Goad, M. R. & Swift-XRT Team 2022, GCN, 31349, 1
Pei, Y. C. 1992, ApJ, 395, 130
Perley, D. A. 2022a, GCN, 31357, 1
Perley, D. A. 2022b, GCN, 31425, 1
Planck Collaboration, Ade, P. A. R., Aghanim, N., et al. 2014, A&A, 571, A16
Rastinejad, J. C., Gompertz, B. P., Levan, A. J., et al. 2022, Natur, 612, 223
Rees, M. J., & Meszaros, P. 1992, MNRAS, 258, 41
Roming, P. W. A., Kennedy, T. E., Mason, K. O., et al. 2005, SSRv, 120, 95
Ryan, G., van Eerten, H., Piro, L., & Troja, E. 2020, ApJ, 896, 166
Saccardi, A., Vergani, S. D., De Cia, A., et al. 2023, A&A, 671, A84
Salvaterra, R. 2015, JHEAp, 7, 35
Sari, R., Piran, T., & Narayan, R. 1998, ApJL, 497, L17
Schlafly, E. F., & Finkbeiner, D. P. 2011, ApJ, 737, 103
Skrutskie, M. F., Cutri, R. M., Stiening, R., et al. 2006, AJ, 131, 1163
Sobral, D., Matthee, J., Darvish, B., et al. 2015, ApJ, 808, 139
Stecklum, B., Eislöffel, J., Klose, S., et al. 2016, Proc. SPIE, 9908, 99084U
Thöne, C. C., Fynbo, J. P. U., Goldoni, P., et al. 2013, MNRAS, 428, 3590
Tody, D. 1986, Proc. SPIE, 627, 733
Tohuvavohu, A., Gropp, J. D., Kennea, J. A., et al. 2022, GCN, 31347, 1
Tomasella, L., Brocato, E., D'Onofrio, M., Cappellaro, E., & Benetti, S. 2022, GCN, 31363, 1
Tsvetkova, A., Frederiks, D., Lysenko, A., et al. 2022, GCN, 31433, 1
Ursi, A., Menegoni, E., Longo, F., et al. 2022a, GCN, 31354, 1
Ursi, A., Romani, M., Piano, G., et al. 2022b, ApJ, 933, 214
Van Rossum, G., & Drake, F. L. 2009, Python 3 Reference Manual (Scotts Valley, CA: CreateSpace)
Virtanen, P., Gommers, R., Oliphant, T. E., et al. 2020, NatMe, 17, 261
Woosley, S. E., & Bloom, J. S. 2006, ARA&A, 44, 507
Zhang, B. 2018, The Physics of Gamma-Ray Bursts (Cambridge: Cambridge Univ. Press)
Zhang, B., Zhang, B.-B., Virgili, F. J., et al. 2009, ApJ, 703, 1696
Zhang, B. B., Liu, Z. K., Peng, Z. K., et al. 2021, NatAs, 5, 911
Zhu, Z.-P., Xu, D., Fynbo, J. P. U., et al. 2023, ApJ, 948, 30
Zou, Y. C., Dai, Z. G., & Xu, D. 2006, ApJ, 646, 1098